

<https://doi.org/10.1038/s44298-024-00063-z>

Potent neutralization by a RBD antibody with broad specificity for SARS-CoV-2 JN.1 and other variants



Michael S. Piepenbrink^{1,9}, Ahmed Magdy Khalil^{2,3,8,9}, Ana Chang^{1,4}, Ahmed Mostafa^{2,5}, Madhubanti Basu¹, Sanghita Sarkar¹, Simran Panjwani⁶, Yaelyn H. Ha¹, Yao Ma², Chengjin Ye², Qian Wang⁷, Todd J. Green⁶, James L. Kizziah⁶, Nathaniel B. Erdmann¹, Paul A. Goepfert¹, Lihong Liu⁷, David D. Ho⁷, Luis Martinez-Sobrido², Mark R. Walter⁶ & James J. Kobbie¹ ✉

SARS-CoV-2 continues to be a public health burden, driven in-part by its continued antigenic diversification and resulting emergence of new variants. By increasing herd immunity, current vaccines have improved infection outcomes for many. However, prophylactic and treatment interventions that are not compromised by viral evolution of the Spike protein are still needed. Using a differential staining strategy with a rationally designed SARS-CoV-2 Receptor Binding Domain (RBD)–ACE2 fusion protein and a native Omicron RBD protein, we developed a recombinant human monoclonal antibody (hmAb) from a convalescent individual following SARS-CoV-2 Omicron infection. The resulting hmAb, 1301B7 potently neutralized a wide range of SARS-CoV-2 variants including the original Wuhan-1, the more recent Omicron JN.1 strain, and SARS-CoV. 1301B7 contacts the ACE2 binding site of RBD exclusively through its VH1-69 heavy chain. Broad specificity is achieved through 1301B7 binding to many conserved residues of Omicron variants including Y501 and H505. Consistent with its extensive binding epitope, 1301B7 is able to potently diminish viral burden in the upper and lower respiratory tract and protect mice from challenge with Omicron XBB1.5 and Omicron JN.1 viruses. These results suggest 1301B7 has broad potential to prevent or treat clinical SARS-CoV-2 infections and to guide development of RBD-based universal SARS-CoV-2 prophylactic vaccines and therapeutic approaches.

Severe Acute Respiratory Syndrome Corona Virus 2 (SARS-CoV-2) is the causative agent of Coronavirus Disease 2019 (COVID-19) which emerged in December 2019 in Wuhan, Hubei Province, China¹. Although the World Health Organization no longer considers COVID-19 a Public Health Emergency of International Concern, it continues to be a significant health threat, with over 300,000 deaths worldwide in 2023². In the United States, COVID-19 has gone from the third leading cause of death in 2021 down to the tenth in 2023. The reduction in COVID-19 related deaths can likely be attributed to better treatment options and increased immunity as a result of

vaccination and/or previous infection. Current COVID-19 vaccines however are sub-optimal in preventing infection, albeit a high bar for respiratory viral infections, and inducing sufficient neutralizing antibodies recognizing conserved epitopes in the viral Spike (S) glycoprotein.

With the initial emergence of the SARS-CoV-2 Omicron variant of concern (VoC) in 2021, greater vaccine breakthrough and reinfection of previously infected individuals was observed³. This was in large part due to numerous mutations in the viral S protein, particularly in the receptor binding domain (RBD) which allowed for immune evasion. Each mutation

¹Department of Medicine, Division of Infectious Diseases, University of Alabama at Birmingham, Birmingham, AL, USA. ²Department of Disease Intervention and Prevention, Texas Biomedical Research Institute, San Antonio, TX, USA. ³Department of Zoonotic Diseases, Faculty of Veterinary Medicine, Zagazig University, Zagazig, Egypt. ⁴Pacific Northwest University of Health Sciences, Yakima, WA, USA. ⁵Center of Scientific Excellence for Influenza Viruses, National Research Centre, Giza, 12622, Egypt. ⁶Department of Microbiology, University of Alabama at Birmingham, Birmingham, AL, USA. ⁷Aaron Diamond AIDS Research Center, Columbia University Vagelos College of Physicians and Surgeons, New York, NY, USA. ⁸Present address: Department of Biomedical Sciences, The College of Medicine, Florida State University, Tallahassee, FL, USA. ⁹These authors contributed equally: Michael S. Piepenbrink, Ahmed Magdy Khalil.

✉ e-mail: jjkobbie@uabmc.edu

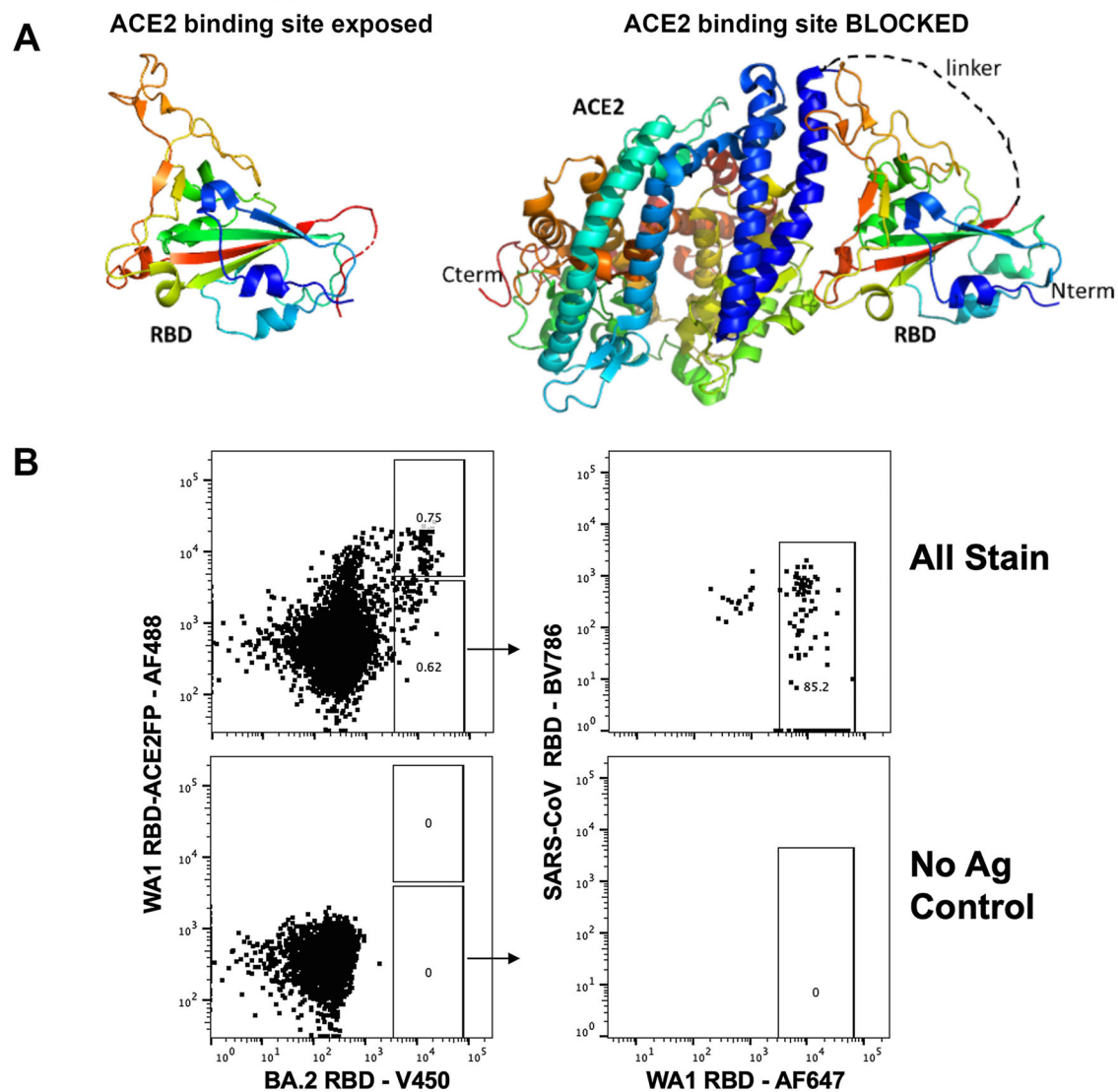


Fig. 1 | RBD-ACE2 stabilized fusion protein for isolation of B cells. A Representation of stabilized WA-1 RBD-ACE2 fusion protein. **B** Strategy for isolation of RBD-specific B cells by flow cytometry. Initial plot gated on live, annexin V negative, CD19 +, IgD negative, HIV p24 negative, peripheral blood B cells.

has the potential of reducing the effectiveness of pre-existing immunity afforded by previous vaccination or SARS-CoV-2 infection. JN.1, a sub-lineage of the BA.2.86 Omicron lineage, distinguished by the L455S mutation in the S protein and three non-S mutations, was the dominant circulating lineage in early 2024⁴. JN.1 appears to have a significant growth advantage when compared to other Omicron lineages (BA.2.86.1, XBB, and HK.3) and the L455S mutation results in considerable immune evasion^{4,5}. This emphasizes the need for updated vaccines to minimize breakthrough infections caused by JN.1 and future SARS-CoV-2 variants.

Despite reductions in SARS-CoV-2 infections; for certain individuals that are either immunocompromised or have comorbidities that increase the risk of progression of disease, the need for therapies is still essential. Although antivirals like nirmatrelvir/ritonavir and molnupiravir are available, conditions like immune system related diseases or cancer may preclude patients from receiving these drugs. Monoclonal antibodies (mAb) are generally safe with few side effects and several targeting the RBD of SARS-CoV-2 S were previously given emergency use authorization by the United States FDA. However, mAb therapies like Evusheld [tixagevimab (AZD8895) and cilgavimab (AZD1061); AstraZeneca] and Sotrovimab (S309) (Glasko Smith Kline) have reduced neutralizing activity against SARS-CoV-2 Omicron, and authorization was subsequently removed. Several notable RBD mutations in recent Omicron variants including

L455S, F456L, and F486P have been suggest to be substantial contributors to neutralizing antibody escape^{6–8}. There are encouraging pre-clinical results for broadly neutralizing universal beta-coronavirus mAbs tolerant of the diversity of Omicron, largely targeting conserved epitopes in the S2 domain of S^{9,10}. However, the development and characterization of RBD-targeting broadly neutralizing Abs that are active against emerging Omicron variants is required to advance new potential therapeutics and to inform future vaccine development.

Here we characterize a fully human mAb (hmAb), 1301B7 derived from a convalescent patient following Omicron infection in the spring of 2023. This 1301B7 hmAb has sub-nanomolar binding to the RBD of the Wuhan-Hu1 strain as well as all Omicron sub-variants tested through a unique heavy chain only binding modality. 1301B7 mediates potent viral neutralization in vitro and prophylactic protection in mice.

Results

RBD-ACE2 fusion protein-base B cell isolation

To identify and enrich for B cells that recognize epitopes within RBD that are involved with ACE2 binding, we developed a negative selection strategy using a RBD-ACE2 fusion protein complex (RBD-ACE2FP), that occludes critical ACE2 binding residues of RBD (Fig. 1A). Using fluorescent streptavidin-tetramer probes of wild type RBDs and the RBD-ACE2FP, a

differential staining strategy was utilized to selectively isolate peripheral blood memory B cells from convalescent individuals following presumed infection with SARS-CoV-2 Omicron which bind WA1 RBD and Omicron BA.2 RBD, but not the RBD-ACE2FP (Fig. 1B, Supplemental Fig. 1). The resulting B cells were used to generate recombinant fully human IgG1 mAbs (hmAbs).

1301B7 hmAb potently binds and neutralizes SARS-CoV-2 variants

Three hmAbs with strong RBD binding emerged from initial screening. hmAbs 1300F12, 1301A8, and 1301B7 all bound RBD V483, RBD L452R T478K, and Wuhan-Hu-1 S well in the presence of 8 M Urea, a chaotropic agent to discern strong antibody binding (Fig. 2A). 1301B7 exhibited the broadest binding profile including recognition of RBD from recent Omicron variants (XBB.1.5, XBB.1.16, EG.5.1, and FL.1) as well as binding of SARS-CoV S protein, with minimal off-target (HIV p24) binding and was advanced for further analysis. Surface plasmon resonance (SPR) indicated 1301B7 had minimal binding to RBD-ACE2FP as expected, and high affinity for WU-1 and Omicron variant RBDs ($K_D = 5\text{--}100\text{ pM}$), with tolerance for variability at key 417, 456, and 487 residues (Fig. 2B). The ability of 1301B7 to compete with ACE2 for binding to SARS-CoV-2 RBD was confirmed by ELISA (Supplemental Fig. 2). The ability of 1301B7 to bind to SARS-CoV-2 infected cells, including JN.1 was confirmed by immunofluorescence (Supplemental Fig. 3). The functional activity of 1301B7 was tested in pseudovirus (Fig. 2C) and live virus (Fig. 2D) -based neutralization assays. Previously described RBD mAbs 25F9¹¹, C68.61¹², and S309¹³ were included as controls. 1301B7 neutralized all SARS-CoV-2 isolates tested, in addition to exhibiting neutralizing activity against SARS-CoV pseudovirus. 1301B7 had superior ability to neutralize the recent Omicron variant JN.1 compared to 25F9, C68.61, and S309. These results indicate that 1301B7 has broad and potent in vitro binding and neutralizing activity against SARS-CoV-2.

Molecular characteristics of 1301B7 hmAb

1301B7 was isolated from an IgG1 expressing B cell and utilizes IGHV1-69 and IGLV1-40 with substantial somatic hypermutation including 20.0% amino acid mutation from germline in the heavy chain variable region, and 14.4% amino acid mutation from germline in the light chain variable region (Table 1, Supplemental Fig. 4). Interestingly, it has a long CDRH3 of 21 amino acids.

Structural characterization of the 1301B7 RBD binding epitope

The cryo-EM structure of 1301B7 Fab bound to trimeric EG.5.1 S was determined to an overall resolution of 3.1 Å (Supplemental Fig. 5 and Supplemental Fig. 6). One 1301B7 Fab binds to the single “up” RBD conformation of the Spike trimer forming a 1Fab : 1S trimer stoichiometry. Due to variability in orientations of the upRBD-Fab complex relative to the rest of the S, the complex was subjected to local refinement, resulting in a 4.1 Å resolution map (Supplemental Fig. 5, Fig. 3A). Map quality was sufficient to trace the Fab heavy chain loops and sidechains to gain insight into the 1301B7 binding epitope. The structure reveals 1301B7 predominantly (73% residue overlap with the ACE2 binding site, defined by pdbid 6m0j) contacts the ACE2 binding region of RBD (825Å²) exclusively through its heavy chain CDRs and FR3 region (Fig. 3B). As previously reported for a VH1-69 anti-influenza HA receptor binding site antibody (F045-092)¹⁴, 1301B7 light chain (LC) residues are ~14 Å away from the RBD. However, the space between RBD and the 1301B7 LC is filled with carbohydrate, donated from the N-linked glycosylation site (Asn100E), located within CDRH3 (Fig. 3A, B). Only the chitobiose core (GlcNAc₂) is observed in the electron density. The GlcNAcs attached to CDRH3 do not form specific contacts with RBD, since the closest h-bonding atom pair (A475 O: O7 GlcNAc) is 4.3 Å apart from one another. However, with subtle conformational changes it is possible that the chitobiose core could form at least transient glycan-RBD interactions that would be independent of heterogeneity in overall mannose composition of the glycan.

A total of 11 hydrogen bond and salt bridge interactions are observed between 1301B7 and RBD (Figs. 3D, E, F, G). CDRH1 forms contacts with RBD residues R403, Y453 and H505 (Supplemental Fig. 4). Notably, FR3 residue Y74, which is a somatic mutation buries the greatest amount of surface area (113 Å²) of any residue in the interface and forms a hydrogen bond network with RBD residues S494, R498, and Y501. Signature VH1-69 hydrophobic residues¹⁵ (I53, L54) at the tip of CDRH2 pack against RBD residues Y489, L456, and L455. CDRH3 buries the most surface area of any CDR into RBD and forms three h-bonds with N417, Y421 and L455. The large number of contacts in the interface is consistent with the high affinity of 1301B7 for the EG.5.1 RBD and may partly explain its broad specificity for multiple SARS-CoV-2 variants. While the RBD N417K mutant results in a ~20-fold drop in 1301B7 affinity, the Ab still retains sub-nanomolar binding affinity for the mutant ($K_D = 100\text{ pM}$) (Fig. 2B). Thus, 1301B7 CDRs may be able to adapt to variations in RBD sequence and structure, while maintaining high affinity and neutralizing potency.

1301B7 hmAb protects from lethal SARS-CoV-2 XBB.1.5 infection

The K18 human ACE2 transgenic mouse model was used to determine the prophylactic activity of 1301B7 hmAb against a lethal infection with the recent SARS-CoV-2 Omicron variant XBB.1.5. Mice were treated with a single intranasal (IN) dose of 10 mg/kg or 1 mg/kg of 1301B7 6 h prior to IN challenge with 10⁵ plaque-forming units (PFU) of XBB.1.5. All mock and isotype control hmAb treated mice exhibited substantial weight loss and had to be euthanized by day 8 post-infection (p.i.), in contrast all 1301B7 hmAb treated mice maintained their body weight and survived (Fig. 4A, B). Treatment with 1 and 10 mg/kg significantly increased survival ($p = 0.003$) as compared to the isotype control mAb treated mice. Treatment with 10 mg/kg of 1301B7 hmAb limited virus in the nasal turbinate, with no detectable virus at day 2 p.i. in any of the mice, and only 1 (out of 4) mouse having detectable virus in the nasal turbinate at day 4 p.i. (Fig. 4C). No detectable virus was evident in the lungs at day 2 or 4 p.i. of mice treated with 10 mg/kg of 1301B7 hmAb (Fig. 4D). Treatment with 1 mg/kg of 1301B7 resulted in modest, but not significant reduction in virus in nasal turbinate, however only 1 (out of 4) mouse had detectable virus in the lungs at day 2 and day 4 p.i.. These results indicate that treatment with 1301B7 hmAb protects from XBB.1.5 infection, and suggests it prevents development of viral replication in the lungs.

1301B7 hmAb protects from SARS-CoV-2 JN.1 infection

We next sought to determine the prophylactic activity of 1301B7 against JN.1 which gained predominance worldwide in late 2023. K18 hACE2 mice were IN treated with 1301B7 6 h prior to challenge with 10⁵ PFU JN.1. Unlike XBB.1.5, untreated JN.1 infected mice had minimal weight loss, and limited mortality, with only a single mouse each from the untreated control and isotype control mAb treated groups required euthanasia (Fig. 5A, B). Mice treated with 2 mg/kg or 20 mg/kg of 1301B7 did not exhibit any weight loss or death. Viral burden was evident in the nasal turbinate and lungs of mock and isotype control hmAb treated mice (Fig. 5C, D). Mice treated with 2 mg/kg and 20 mg/kg of 1301B7 hmAb had a significant reduction ($p < 0.05$) in nasal turbinate virus at day 2 p.i. compared to isotype control hmAb treated mice, with the significant reduction persisting at day 4 p.i. in those treated with 20 mg/kg of 1301B7. Both doses of 1301B7 resulted in significant reduction in lung virus at day 2 and day 4 p.i., with only 1 (out of 4) mouse having detectable virus in each group at day 2 p.i. At day 4 p.i. no mice treated with 20 mg/kg of 1301B7 had detectable virus in the lungs, and only 1 (of 4) mouse treated with 2 mg/kg of 1301B7 having detectable virus in the lungs. Together these results indicate that 1301B7 has potent prophylactic activity against multiple SARS-CoV-2 Omicron variants, including the latest circulating XBB.1.5 and JN.1 strains.

Discussion

SARS-CoV-2 is now thoroughly entrenched in humanity due to its continued ability to subvert pre-existing immunity. Thus, defining its vulnerabilities for targeted development of highly effective next generation

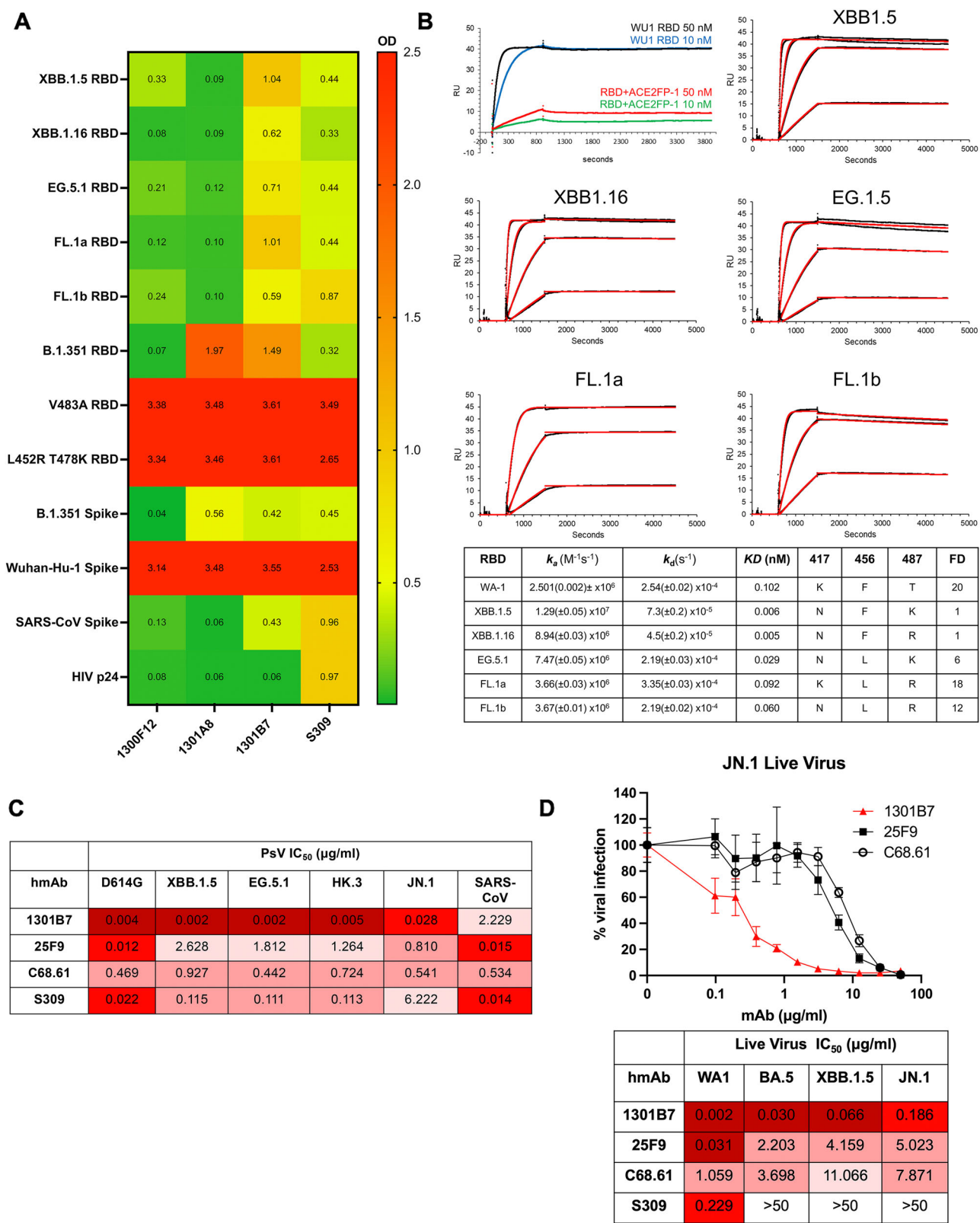


Fig. 2 | SARS-CoV-2 binding and neutralization by 1301B7 hmAb. **A** hmAbs were tested at 1 μg/ml in triplicate for binding to indicated protein in the presence of 8 M urea by ELISA. Average optical density (OD) at 450 nm is shown. **B** Binding to indicated RBD was determined by SPR. Concentrations of the RBDs evaluated are 50, 12.5, 3.125, and 0.781 nM. The 50 nM concentration was not evaluated for 1301B7-FL.1 interactions. Embedded table indicates key amino acid residues and fold difference (FD) relative KD of XBB.1.5. hmAbs were tested at increasing concentrations in triplicate for neutralization by pseudovirus-based (**C**) or live virus (**D**) neutralization assays.

Table 1 | Molecular characteristics of hmAbs

mAb	VH	DH	JH	Isotype	% mutation (AA)	HCDR3 length (AA)	VL	JL	% mutation (AA)	LCDR3 length (AA)
1301B7	IGHV1-69	IGHD4-17	IGHJ6	IgG1	20.0	21	IGLV1-40	IGLJ2	14.4	10
1301A8	IGHV1-69	IGHD1-26	IGHJ2	IgA1	16.7	18	IGKV4-1	IGKJ2	6.4	9
1300F12	IGHV3-66	IGHD3-16	IGHJ6	IgA2	14.4	16	IGLV1-51	IGLJ1	11.2	12

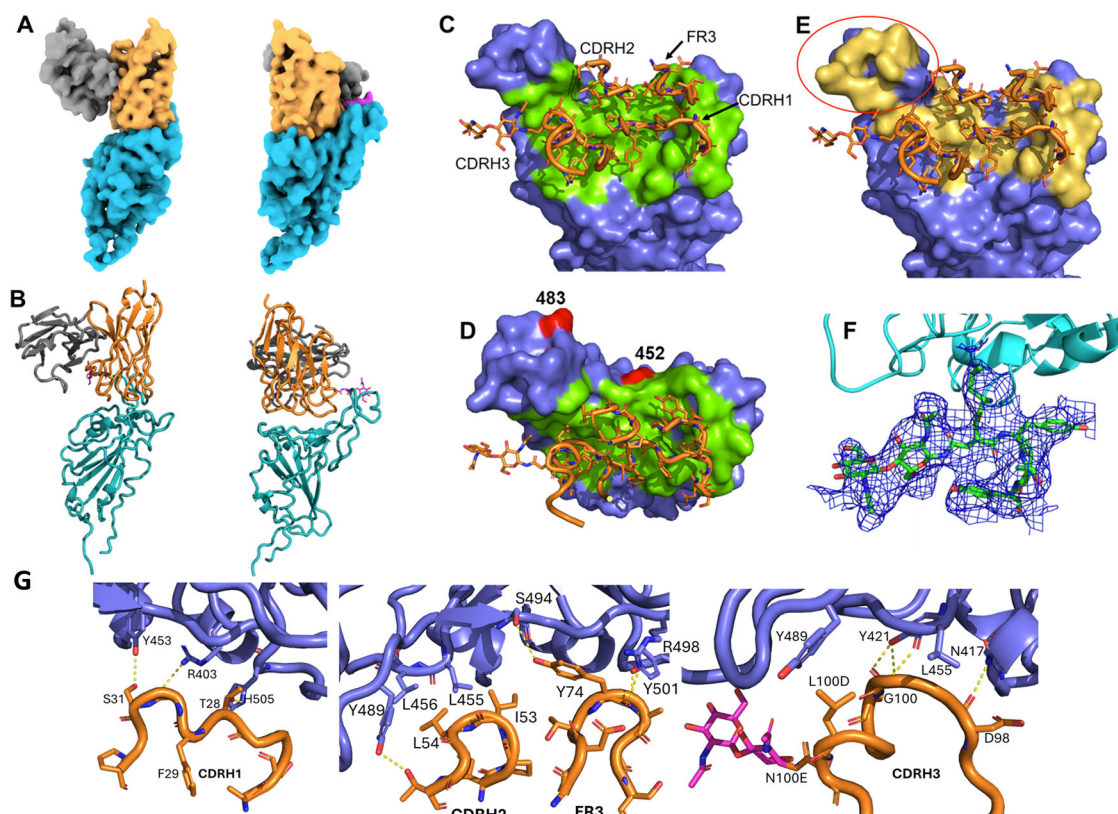


Fig. 3 | Structure of the 1301B7Fab - EG5.1 SARS-CoV-2 Spike. **A** Orthogonal views of the Cryo-EM density for the upRBD-1301B7 Fv complex with RBD cyan, 1301B7 heavy and light chains yellow and grey, respectively, and the glycan attached to CDRH3 is shown in magenta. **B** Ribbon diagram of the final model in the orientations shown in **A**. **(C, D)** Orthogonal views of the 1301B7 RBD binding site shown as a green surface on the EG5.1 RBD, with CDR/FR3 residues colored in

green. The location of two significant JN.1 mutations L452W and V483del are shown in red. **E** 1301B7 CDRs/FR3 contact residues shown on the ACE2 binding surface (yellow) of RBD, showing 1301B7 does not bind to the “tip” region of RBD circled in red on the figure⁴⁰. **F** Electron density from the 4.1 Å local-refined map corresponding to a portion of CDRH3 and the N-linked glycan attached to Asn100E. **G** Molecular interactions between 1301B7 and EG5.1 RBD.

vaccines and therapeutics is critical to meaningful advances in reducing the impact of the virus on human health. Antibody responses to the RBD have consistently been among the most potent in neutralizing SARS-CoV-2 infection and pathogenesis, yet the activity of RBD-targeting antibodies is often negated with the development of new variants that exhibit multiple amino acid changes in the RBD. Despite sensitivity to immune evasion, a subset of RBD mAbs broadly neutralize SARS-CoV-2 variants. Here we have defined 1301B7 as a hmAb capable of broadly neutralizing all SARS-CoV-2 variants it was tested against, as well as SARS-CoV. In direct comparison, 1301B7 in vitro neutralizing activity was similar to other recently described RBD mAbs. Although not directly compared, the ability of 1301B7 to protect from lethal SARS-CoV-2 Omicron XBB1.5 infection at 1 mg/kg and SARS-CoV-2 JN.1 infection at 2 mg/kg suggest it’s in vivo activity is among the most potent hmAbs tested at this time.

While the throughput of screening antigen-specific B cells and the B cell repertoire for neutralizing mAbs continue to increase with improving platforms, the efficiency of such campaigns will still be impacted by the initial selection process. Although we have not expressly tested the efficiency of our RBD-ACE2FP-/RBD+ differential selection approach compared to

standard RBD-based positive selection, we expect it contributed to the successful isolation of 1301B7, which mimics ACE2 and potently competes with ACE2 in its binding to SARS-CoV-2 S protein. Subsequently, further application of this differential selection approach to efficiently identify and stratify RBD-specific B cells, to better define responses to various vaccine regimens, breakthrough infections, and unique patient populations is warranted and may aid in identify those B cells with broad SARS-CoV-2 protective potential.

The structure of 1301B7 bound to the EG5.1 SARS-CoV-2 S revealed 1301B7 binds to RBD exclusively through its heavy chain CDRs and FR3 region to generate a picomolar affinity antibody against SARS-CoV-2 variants. Consistent with its novel structure and high binding affinity, 1301B7 uses a VH1-69 heavy chain that has been shown to be elicited against the endemic viruses influenza, hepatitis, HIV-1¹⁵, as well as SARS-CoV-2¹⁶. To our knowledge, this is the first VH1-69 SARS-CoV-2 NAb that exclusively uses the heavy chain and contains an N-linked glycosylation site in CDRH3. N-linked glycosylation within the variable region is estimated to occur in about 15–25% of human IgG Abs, and have been shown to influence specificity and affinity^{17–19}. There are a few examples of N-linked glycosylation

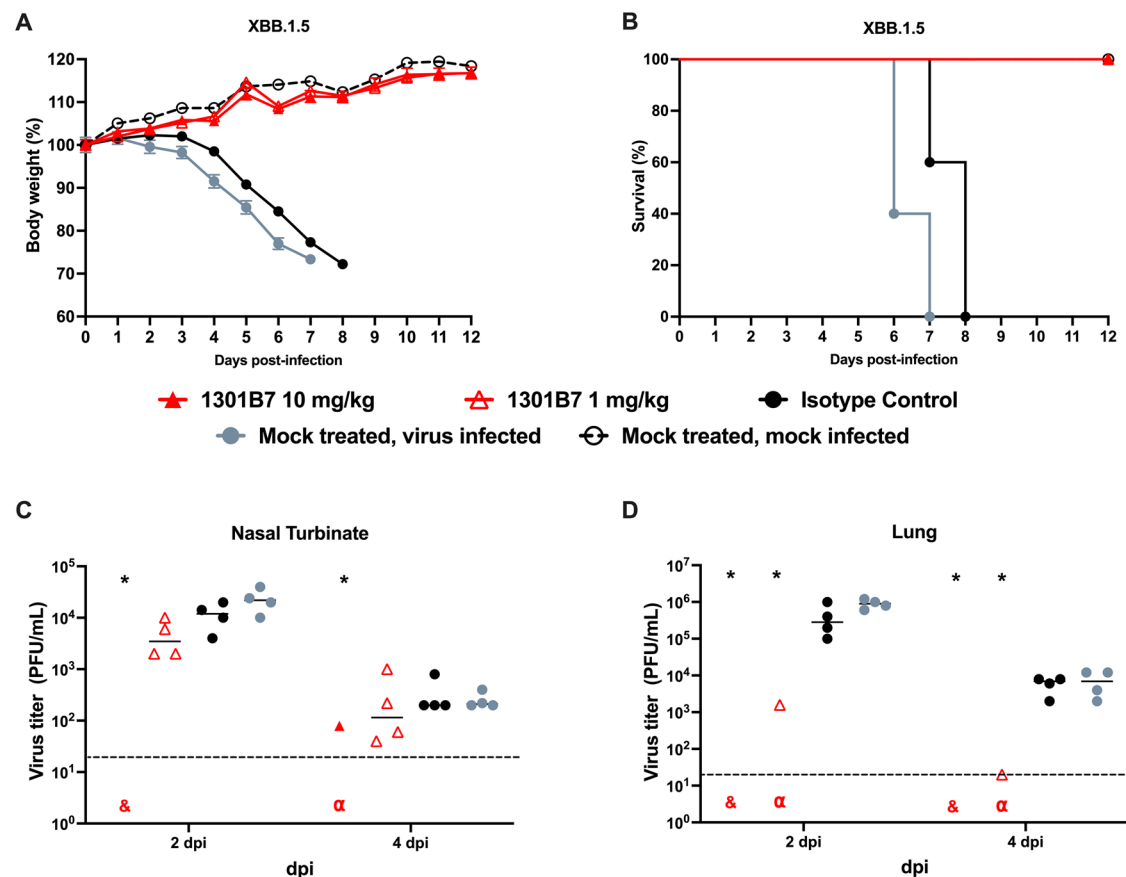


Fig. 4 | Prophylactic activity of 1301B7 hmAb against SARS-CoV-2 XBB.1.5. K18 hACE2 transgenic mice were treated i.n. with 1301B7 (1 mg/kg or 10 mg/kg) or isotype control hmAb (10 mg/kg), followed by infection with 10^5 PFU SARS-CoV-2 XBB.1.5. Body weight (A) and survival (B) were evaluated at the indicated days post-infection ($n = 5$ mice/group). Mice that lost >25% of their initial body weight were humanely euthanized. Error bars represent standard error of the mean (SEM) for

each group of mice. Viral titers in the nasal turbinate (C) and lung (D) at 2 and 4 days p.i. were determined by plaque assay in Vero AT cells ($n = 4$ mice/group/day). Symbols represent individual mice, bars indicate the mean of virus titers. Dotted lines indicate limit of detection. & indicates virus not detected in any mice from that group. α indicates virus detected in only one mouse from that group. * indicates $p < 0.05$ as compared to isotype control hmAb as determined by t -test.

improving Ab affinity, however N-linked glycans in CDRH3 often have no effect on or reduce affinity^{20–22}. For 1301B7, the glycan attached to CDRH3 fills the cavity between the diminutive light chain and the RBD, providing a structural scaffold to design novel broad-specificity antibodies using protein, as well as glycan-based engineering strategies. The broad specificity of 1301B7 appears to be a combination of a sub-nanomolar NAb that forms multiple h-bonds, with many other CDR residues poised to accommodate mutational variation in the RBD. Confirmation of the proposed mechanism of broad specificity, as well as the specific requirements of hmAb somatic mutations to further understand the incidence and ability to induce these broadly neutralizing Abs through targeted vaccine strategies will be the focus of future studies.

Among SARS-CoV-2 Omicron variants there has been substantial variability in their ability to cause significant morbidity and mortality in K18 hACE2 mice^{23–25}. Observing that all untreated animals challenged with 10^5 PFU XBB.1.5 had rapid weight loss that required euthanasia, it was unexpected that the same dose of JN.1 resulted in minimal weight loss and only 20% mortality. Nasal and lung viral titers were similar in the untreated animals between viruses, suggesting mortality was not a consequence of any gross difference in viral replication dynamics, and further determination if aspects such as inflammatory burden or secondary sites (brain, gut) may differ between the variants.

The ability of 1301B7 to limit viral titers to be below the detection limit in many of the mice is encouraging and may suggest the potential to limit transmission which warrants direct assessment. It also indicates that the potential for optimal dosing of 1301B7 to mediate sterilizing protection

from SARS-CoV-2 exposure should be thoroughly assessed. As we have previously demonstrated the benefits of direct respiratory delivery of mAbs for treatment of SARS-CoV-2 infection in mice, hamsters, and rhesus macaques^{26–28}, extending the utility of this approach here to recent SARS-CoV-2 variants, including JN.1, further supports its advancement for clinical prophylaxis and treatment of SARS-CoV-2 infections.

Materials and methods

Ethics statement

All procedures and methods involving human samples were approved by the Institutional Review Board for Human Use at the University of Alabama at Birmingham (IRB-160125005). Written or oral informed consent was obtained from the participants. All experiments were performed in accordance with relevant guidelines and regulations.

Biosafety

All in vitro and in vivo experiments with live SARS-CoV-2 were conducted in appropriate biosafety level (BSL) 3 and animal BSL3 (ABSL3) laboratories at Texas Biomedical Research Institute with approval from Biosafety (BSC), recombinant DNA (RDC), and Animal Care and Use (IACUC) committees.

Cells and viruses

Vero E6 cells (BEI Resources NR-54970) expressing hACE2 and TMPRSS2 (Vero AT cells) were grown in Dulbecco's modified Eagle's medium (DMEM; Corning, Mediatech, Inc. Durham, NC, USA) supplemented with

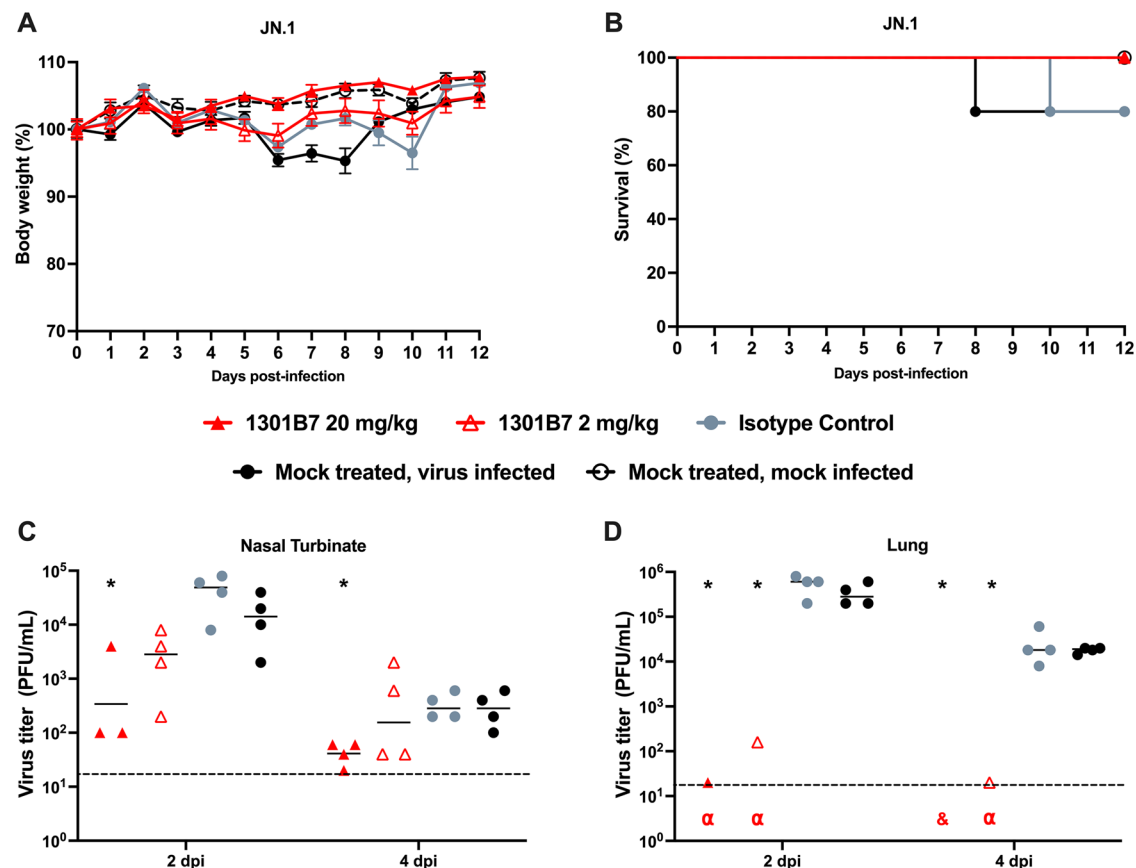


Fig. 5 | Prophylactic activity of 1301B7 hmAb against SARS-CoV-2 JN.1. K18 hACE2 transgenic mice were treated i.n. with 1301B7 (2 mg/kg or 20 mg/kg) or isotype control hmAb (20 mg/kg), followed by infection with 10^5 PFU SARS-CoV-2 JN.1. Body weight (A) and survival (B) were evaluated at the indicated days post-infection ($n = 5$ mice/group). Mice that lost >25% of their initial body weight were humanely euthanized. Error bars represent standard error of the mean (SEM) for

each group of mice. Viral titers in the nasal turbinate (C) and lung (D) at 2 and 4 days p.i. were determined by plaque assay in Vero AT cells ($n = 4$ mice/group/day). Symbols represent individual mice, bars indicate the mean of virus titers. Dotted lines indicate limit of detection. & indicates virus not detected in any mice from that group. α indicates virus detected in only one mouse for that group. * indicates $p < 0.05$ as compared to isotype control hmAb as determined by t -test.

5% fetal bovine serum (FBS, VWR) and 1% PSG (penicillin, 100 units/mL; streptomycin, 100 μ g/mL; L-glutamine, 2 mM, Corning, Mediatech, Inc.) at 37 °C with 5% CO₂. For SARS-CoV-2 infection, Vero AT cells were maintained in post-infection medium (DMEM supplemented with 2% FBS and 1% PSG) and incubated at 37 °C with 5% CO₂. SARS-CoV-2 WA1 was obtained from BEI Resources (NR-52281). SARS-CoV-2 Omicron BA.5 (NR-58620), XBB1.5 (NR-59105), and JN.1 (NR-59694) were generously provided by Dr. Clint Florence, Program Officer, Office of Biodefense, Research Resources, and Translational Research at NIH/NIAID/DMID/OBRRTR/RRS.

B cell isolation and hmAb generation

Peripheral blood was collected at the University of Alabama at Birmingham from adult convalescent patients approximately one month following PCR confirmed infection with SARS-CoV-2 in 2023. Peripheral blood mononuclear cells (PBMC) were isolated by density gradient centrifugation and cryopreserved. RBD-ACE2FP consists of RBD (Wuhan-1) residues 333–518 and ACE2 residues 20–598, joined by a 19 amino acid linker. RBD-ACE2FP was confirmed to have the correct size by SDS-PAGE and reactivity profile by SPR. Biotinylated RBD and RBD-ACE2FP proteins were used to create fluorescent streptavidin tetramers as previously described²⁷. Cryopreserved cells were thawed and then stained for flow cytometry similar as previously described in ref.¹⁸, using HIV p24-PE, RBD-ACE2FP-SA-AlexaFluor488, WA1 RBD-SA-AlexaFluor647, BA.2 RBD-SA-BV450, SARS-CoV1 RBD-SA-BV786, CD3-BV510 (OKT3, Biolegend), CD4-BV510 (HI30, Biolegend), CD14-BV510 (63D3, Biolegend), anti-CD19-APC-Cy7 (SJ25C1, BD

Biosciences), IgD-PE-Cy7 (IA6-2, Biolegend), Annexin V-PerCP-Cy5.5 (Biolegend), and Live/Dead aqua (Molecular Probes). Single B cells were sorted using a FACSMelody (BD Biosciences) into 96-well PCR plates containing 4 μ l of lysis buffer as previously described in ref.³⁷. Plates were immediately frozen at -80 °C after sorting until thawed for reverse transcription and nested PCR performed for IgH, Ig λ , and Ig κ variable gene transcripts as previously described^{29,30}. Immunoglobulin sequences were analyzed by IgBlast (www.ncbi.nlm.nih.gov/igblast) and IMGT/V-QUEST (http://www.imgt.org/IMGT_vquest/vquest) to determine which sequences should lead to productive immunoglobulin, to identify the germline V(D)J gene segments with the highest identity, and to scrutinize sequence properties. Paired heavy and light chain genes were cloned into IgG1 expression vectors and were transfected into HEK293T cells and culture supernatant was concentrated using 100,000 MWCO Amicon Ultra centrifugal filters (Millipore-Sigma, Cork, Ireland), and IgG captured and eluted from Magne Protein A beads (Promega, Madison, WI) as previously described^{29,30}. 25F9 and C68.61 were previously described^{11,12} and heavy and light chain variable regions synthesized by Twist Biosciences on reported sequences and cloned into IgG1 expression vector for production in HEK293T cell.

Binding characterization

Recombinant proteins used include SARS-CoV-2 RBD WU1, RBD XBB1.5, RBD XBB.1.16, RBD EG.5.1, RBD FL.1a, and RBD FL.1b produced in house (Supp Fig. 1), and RBD B.1.351 (BEIR, NR-55278), RBD V483A (Acros, SPD-C52H5), RBD L452R T478K (Sino, 40592-V08H90), Spike Wuhan-Hu-1 (BEIR, NR-52308), SARS-CoV1 Spike (BEIR, NR-686), and

HIV p24 (Abcam, ab43037). ELISA plates (Nunc MaxiSorp; Thermo Fisher Scientific, Rochester, NY) were coated with recombinant CoV proteins at 1 µg/ml. Purified hmAbs were diluted in PBS, added to ELISA plate and incubated for 1 h followed by 8 M urea treatment for 15 minutes. Binding was detected with HRP-conjugated anti-human IgG (Jackson ImmunoResearch, West Grove, PA). SPR experiments were performed on a Biacore T200 (Cytiva) at 25 °C using a running buffer consisting of 10 mM HEPES, 150 mM NaCl, 0.0075% P20. Kinetic binding analysis for 1301B7 was performed by capturing the hmAbs to the chip surface of CM-5 chips using a human antibody capture kit (Cytiva). The binding kinetics for the interaction between hmAbs and SARS-CoV-2 Spike protein (R&D Systems, 10549-cv) was determined by injecting two to four concentrations of SARS-CoV-2 RBD (50 nM highest concentration). All SPR experiments were double referenced (e.g., sensorgram data was subtracted from a control surface and from a buffer blank injection). The control surface for all experiments consisted of the capture antibody. Sensorgrams were globally fit to a 1:1 model, without a bulk index correction, using Biacore T-200 evaluation software version 1.0.

Neutralization

hmAbs were tested for neutralization of live SARS-CoV-2 variants as previously described³¹. A mixture of serially diluted hmAb (starting concentration of 50 µg/ml) and 200 PFU/well of SARS-CoV-2 in post-infection media were incubated at 37 °C and 5% CO₂. After 1 h incubation, Vero AT cells (96-well plate format, 4 × 10⁴ cells/well, quadruplicates) were infected with the hmAb-virus mixture. After 1 h of viral adsorption, the mixture overlay was changed with 100 µl of post-infection media containing 1% Avicel. At 18 h p.i. (14 h p.i. for WA1 strain), infected cells were fixed with 10% neutral formalin for 24 h and immunostained with the anti-NP monoclonal antibody 1C7C7³¹. Virus neutralization was quantified using an ELISPOT plate reader, and the percentage of infectivity calculated using sigmoidal dose response curves. The formula to calculate percent viral infection for each concentration is given as [(Average # of plaques from each treated wells—average # of plaques from “no virus” wells)/(average # of plaques from “virus only” wells—average # of plaques from “no virus” wells)] × 100. A non-linear regression curve fit analysis over the dilution curve was performed using GraphPad Prism to calculate NT₅₀. Mock-infected cells and viruses in the absence of hmAb were used as internal controls.

hmAbs were also tested using a S-pseudotyped virus (PsV) assay. Pseudotyped SARS-CoV-2 was generated using a protocol established previously³². Initially, HEK293T cells were transfected with SARS-CoV-2 S-encoding plasmids using 1 mg/ml of PEI and cultured for 24 h. Following this, the transfected HEK293T cells were infected with VSV-G pseudotyped ΔG-luciferase virus (Kerafast, EH1020-PM) at a multiplicity of infection (MOI) of approximately 3 to 5. After a 2 h incubation, the cells were washed three times with complete culture medium and were subsequently maintained in fresh medium for an additional 24 h. The transfection supernatant was then harvested and clarified by centrifugation at 2000 rpm for 10 min. Each viral stock was subsequently incubated with 20% I1 hybridoma (ATCC, CRL-2700) supernatant for 1 h at room temperature to neutralize contaminating VSV-G particle before measuring titers and making aliquots for storage at −80 °C until use. Pseudoviruses were subjected to titration to standardize the viral input prior to each neutralization assay. hmAbs were diluted from an initial concentration of 20 µg/ml by a factor of five in 96-well plates, in triplicates. Subsequently, 50 µL of each dilution of mAb was incubated with 50 µL of diluted pseudovirus for 1 h at 37 °C, followed by the addition of 100 µL of resuspended Vero-E6 cells at a density of 3 × 10⁶ cells/ml. Wells without mAbs (serving as ‘virus alone’ controls) were included in all plates. The plates were then incubated at 37 °C overnight before the quantification of luciferase activity using the Luciferase Assay System (Promega) on Soft-Max Pro v7.0.2 (Molecular Devices). The reduction in luciferase activity for each mAb dose, compared with the ‘virus alone’ controls, was calculated. Neutralization IC₅₀ values for the mAbs were obtained by fitting the

data to a nonlinear five-parameter dose-response curve using GraphPad Prism v9.2.

Cryo-EM structural analysis

DNA for the SARS-CoV-2 EG5.1 S ectodomain with 6 P, furin mutations, and a 6His C-terminal tag was synthesized and placed into the pTwist-CMV expression vector (Twist Bioscience). S Trimer protein was produced by transfecting the plasmid into EXP1293 cells following manufacturer’s instructions. After 6 days, the media was harvested and dialyzed into 20 mM Tris, pH 8, 0.5 M NaCl, 5 mM Imidazole. The S trimer was purified by nickel affinity chromatography (Novagen), followed by gel filtration chromatography. 1301B7Fab was produced by cleavage of the antibody with papain for 7 h. Following cleavage, the FC was removed by protein-A affinity chromatography. The Fab was concentrated/exchanged into 20 mM Hepes, pH 7.5, 50 mM NaCl and separated from uncut mab species by gel filtration chromatography.

The Cryo-EM sample was prepared by heating the S trimer for 10 min at 37 °C, followed by the addition of a 1.3 molar ratio of 1301B7Fab. The sample (3 µl) was immediately added to C-flat R2/1 300 mesh grids placed into an Vitrobot Mark IV at 1.5 mg/ml concentration for 30 s and then blotted for 4–5 s, prior to plunge freezing. Grids were imaged on a Glacios 2 cryo-TEM, outfitted with a Falcon 4i detector using EPU software. All cryo-EM processing, from movies to final refinement, were performed using cryoSPARC v4.4.1³³. Masking and density segmentation were performed using segger³⁴, implemented in ChimeraX³⁵. Model building was performed using cool³⁶ and refinements were performed using Phenix³⁷. Ribbon diagrams were made using pymol³⁸ and chimeraX.

K18 hACE2 transgenic mice experiments

All animal protocols involving K18 hACE2 transgenic mice were approved by the Texas Biomedical Research Institute IACUC (1718MU). Five-week-old female K18 hACE2 transgenic mice were purchased from The Jackson Laboratory and maintained in the BSL3 animal facility at Texas Biomedical Research Institute under specific pathogen-free conditions. Mice were treated with a single dose of hmAb delivered i.n. in a total volume of 50 µl 6 h prior to viral challenge. For virus infection, mice were anesthetized following gaseous sedation in an isoflurane chamber and i.n. inoculated with 50 µl of a viral dose of 10⁵ PFU per mouse. After viral infection, mice were monitored daily for morbidity (body weight) and mortality (survival rate) for 12 days. Mice showing a loss of more than 25% of their initial body weight were defined as reaching the experimental end point and humanely euthanized. Euthanasia performed by administering pentobarbital sodium solution. Nasal turbinate and lungs from mock or infected animals were homogenized in 1 ml of PBS for 20 s at 7,000 rpm using a Precellys tissue homogenizer (Bertin Instruments). Tissue homogenates were centrifuged at 12,000 × g (4 °C) for 5 min, and supernatants were collected and titrated by plaque assay and immunostaining as previously described in ref.³⁹.

Statistical analysis

Significance was determined using GraphPad Prism, v8.0. Kaplan-Meier log rank test was applied for the evaluation of survival between treatments. Two-tailed *t*-tests were applied for evaluation of the viral titer results between treatments. Significance was declared at *p* < 0.05. For statistical analysis viral titers were log transformed and undetectable virus was set to the limit of detection.

Data availability

No datasets were generated or analysed during the current study.

Received: 23 May 2024; Accepted: 1 October 2024;

Published online: 14 November 2024

References

- Holshue, M. L. et al. First Case of 2019 Novel Coronavirus in the United States. *N. Engl. J. Med.* **382**, 929–936 (2020).

2. WHO. WHO COVID-19 dashboard. 2024 [cited 2024] Available from: <https://data.who.int/dashboards/covid19/deaths?n=c>.
3. Arabi, M. et al. Role of previous infection with SARS-CoV-2 in protecting against omicron reinfections and severe complications of COVID-19 compared to pre-omicron variants: a systematic review. *BMC Infect. Dis.* **23**, 432 (2023).
4. Planas, D. et al. Distinct evolution of SARS-CoV-2 Omicron XBB and BA.2.86/JN.1 lineages combining increased fitness and antibody evasion. *Nat. Commun.* **15**, 2254 (2024).
5. Kaku, Y. et al. Virological characteristics of the SARS-CoV-2 JN.1 variant. *Lancet Infect. Dis.* **24**, e82 (2024).
6. Li, P. et al. Neutralization escape, infectivity, and membrane fusion of JN.1-derived SARS-CoV-2 SLIP, FLIRT, and KP.2 variants. *Cell Rep.* **43**, 114520 (2024).
7. Li, W. et al. Key mechanistic features of the trade-off between antibody escape and host cell binding in the SARS-CoV-2 Omicron variant spike proteins. *EMBO J.* **43**, 1484–1498 (2024).
8. Zhang, L. et al. Rapid spread of the SARS-CoV-2 JN.1 lineage is associated with increased neutralization evasion. *iScience* **27**, 109904 (2024).
9. Deshpande, A. et al. Structure and epitope of a neutralizing monoclonal antibody that targets the stem helix of beta coronaviruses. *FEBS J.* **290**, 3422–3435 (2023).
10. Ju, B. et al. Striking antibody evasion of SARS-CoV-2 Omicron sub-lineages BQ.1.1, XBB.1 and CH.1.1. *Nat. Sci. Rev.* **10**, nwad148 (2023).
11. Feng, Y. et al. Broadly neutralizing antibodies against sarbecoviruses generated by immunization of macaques with an AS03-adjuvanted COVID-19 vaccine. *Sci. Transl. Med.* **15**, eadg7404 (2023).
12. Guenthoer, J. et al. Identification of broad, potent antibodies to functionally constrained regions of SARS-CoV-2 spike following a breakthrough infection. *Proc. Natl Acad. Sci. USA* **120**, e2220948120 (2023).
13. Pinto, D. et al. Cross-neutralization of SARS-CoV-2 by a human monoclonal SARS-CoV antibody. *Nature* **583**, 290–295 (2020).
14. Lee, P. S. et al. Receptor mimicry by antibody F045-092 facilitates universal binding to the H3 subtype of influenza virus. *Nat. Commun.* **5**, 3614 (2014).
15. Chen, F., Tzarum, N., Wilson, I. A. & Law, M. V(H)1-69 antiviral broadly neutralizing antibodies: genetics, structures, and relevance to rational vaccine design. *Curr. Opin. Virol.* **34**, 149–159 (2019).
16. He, P. et al. SARS-CoV-2 Delta and Omicron variants evade population antibody response by mutations in a single spike epitope. *Nat. Microbiol.* **7**, 1635–1649 (2022).
17. van de Bovenkamp, F. S., Hafkenscheid, L., Rispens, T. & Rombouts, Y. The Emerging Importance of IgG Fab Glycosylation in Immunity. *J. Immunol.* **196**, 1435–1441 (2016).
18. Arnold, J. N., Wormald, M. R., Sim, R. B., Rudd, P. M. & Dwek, R. A. The impact of glycosylation on the biological function and structure of human immunoglobulins. *Annu Rev. Immunol.* **25**, 21–50 (2007).
19. Wright, A., Tao, M. H., Kabat, E. A. & Morrison, S. L. Antibody variable region glycosylation: position effects on antigen binding and carbohydrate structure. *EMBO J.* **10**, 2717–2723 (1991).
20. van de Bovenkamp, F. S. et al. Adaptive antibody diversification through N-linked glycosylation of the immunoglobulin variable region. *Proc. Natl. Acad. Sci. USA* **115**, 1901–1906 (2018).
21. Coloma, M. J., Trinh, R. K., Martinez, A. R. & Morrison, S. L. Position effects of variable region carbohydrate on the affinity and in vivo behavior of an anti-(1→6) dextran antibody. *J. Immunol.* **162**, 2162–2170 (1999).
22. Song, R., Oren, D. A., Franco, D., Seaman, M. S. & Ho, D. D. Strategic addition of an N-linked glycan to a monoclonal antibody improves its HIV-1-neutralizing activity. *Nat. Biotechnol.* **31**, 1047–1052 (2013).
23. de Campos-Mata, L. et al. A monoclonal antibody targeting a large surface of the receptor binding motif shows pan-neutralizing SARS-CoV-2 activity. *Nat. Commun.* **15**, 1051 (2024).
24. Song, Y. et al. A Synthetic SARS-CoV-2-Derived T-Cell and B-Cell Peptide Cocktail Elicits Full Protection against Lethal Omicron BA.1 Infection in H11-K18-hACE2 Mice. *Microbiol Spectr.* **11**, e0419422 (2023).
25. Rizvi, Z. A. et al. Omicron sub-lineage BA.5 infection results in attenuated pathology in hACE2 transgenic mice. *Commun. Biol.* **6**, 935 (2023).
26. Piepenbrink, M. S. et al. Therapeutic activity of an inhaled potent SARS-CoV-2 neutralizing human monoclonal antibody in hamsters. *Cell Rep. Med.* **2**, 100218 (2021).
27. Piepenbrink, M. S. et al. Potent universal beta-coronavirus therapeutic activity mediated by direct respiratory administration of a Spike S2 domain-specific human neutralizing monoclonal antibody. *PLoS Pathog.* **18**, e1010691 (2022).
28. Streblow, D. N. et al. Aerosol delivery of SARS-CoV-2 human monoclonal antibodies in macaques limits viral replication and lung pathology. *Nat. Commun.* **14**, 7062 (2023).
29. Nogales, A. et al. A Highly Potent and Broadly Neutralizing H1 Influenza-Specific Human Monoclonal Antibody. *Sci. Rep.* **8**, 4374 (2018).
30. Basu, M. et al. Persistence of HIV-1 Env-Specific Plasmablast Lineages in Plasma Cells after Vaccination in Humans. *Cell Rep. Med.* **1**, 100015 (2020).
31. Park, J. G. et al. Rapid in vitro assays for screening neutralizing antibodies and antivirals against SARS-CoV-2. *J. Virol. Methods* **287**, 113995 (2021).
32. Wang, Q. et al. Alarming antibody evasion properties of rising SARS-CoV-2 BQ and XBB subvariants. *Cell* **186**, 279–286.e278 (2023).
33. Punjani, A., Rubinstein, J. L., Fleet, D. J. & Brubaker, M. A. cryoSPARC: algorithms for rapid unsupervised cryo-EM structure determination. *Nat. Methods* **14**, 290–296 (2017).
34. Pintilie, G. D., Zhang, J., Goddard, T. D., Chiu, W. & Gossard, D. C. Quantitative analysis of cryo-EM density map segmentation by watershed and scale-space filtering, and fitting of structures by alignment to regions. *J. Struct. Biol.* **170**, 427–438 (2010).
35. Meng, E. C. et al. UCSF ChimeraX: Tools for structure building and analysis. *Protein Sci.* **32**, e4792 (2023).
36. Emsley, P. & Cowtan, K. Coot: model-building tools for molecular graphics. *Acta Crystallogr D. Biol. Crystallogr* **60**, 2126–2132 (2004).
37. Afonine, P. V. et al. Real-space refinement in PHENIX for cryo-EM and crystallography. *Acta Crystallogr D. Struct. Biol.* **74**, 531–544 (2018).
38. The PyMOL Molecular Graphics System. 3.0 ed: Schrödinger, LLC.
39. Khalil, A. M. et al. Fc-Effector-Independent in vivo Activity of a Potent Influenza B Neuraminidase Broadly Neutralizing Antibody. *Viruses* **15**, 1540 (2023).
40. Deshpande, A., Harris, B. D., Martinez-Sobrido, L., Kobie, J. J. & Walter, M. R. Epitope Classification and RBD Binding Properties of Neutralizing Antibodies Against SARS-CoV-2 Variants of Concern. *Front Immunol.* **12**, 691715 (2021).

Acknowledgements

We are grateful for the clinical research staff that enabled this project and the assistance of the University of Alabama at Birmingham (UAB) Center for AIDS Research, the UAB Flow Cytometry & Single Cell Core Facility, UAB Multidisciplinary Molecular Interaction Core Facility, and UAB Cryo-EM Facility. We thank William Overton for technical assistance. We thank BEI Resources for providing reagents. We also want to thank Dr. Clint Florence, Program Officer, Office of Biodefense, Research Resources, and Translational Research at NIH/NIAID/DMID/OBRRTR/RRS for providing SARS-CoV-2 Omicron BA.5, XBB1.5 and JN.1. We are most grateful for the participation of the study volunteers. Funding for this work provided by institutional support from the UAB (to J.J.K.) and Texas Biomedical Research Institute (to L.M.-S.), National Institutes of Health (1R01AI161175 to J.J.K., L.M.S. and M.R.W.), Center for Research on Influenza Pathogenesis and Transmission (CRIPT), a NIAID-funded Center of Excellence for Influenza Research and Response (CEIRR, contract # 75N93021C00014 to L.M.-S.), and the Coronavirus Prevention Network and HIV Vaccines Trials Network

Research and Mentorship Program (RAMP) (5UM1AI068614 to A.C. and J.J.K.). The UAB Cryo-EM Facility is supported by the Institutional Research Core Program and O'Neal Comprehensive Cancer Center (NIH grant P30 CA013148), with additional funding from NIH grant S10 OD024978. Funders had no role in study design, data collection and analysis, decision to publish, or preparation of the manuscript.

Author contributions

J.J.K., L.M.-S., and M.R.W. conceived the study. M.S.P., A.C., M.B., S.S., and J.J.K. isolated and screened the mAbs. M.S.P., M.B., S.S., Y.H.H., J.J.K., S.P., M.R.W., and S.P. produced the recombinant proteins and conducted SPR. M.R.W., T.G., and J.L.K. conducted the Cryo-Em analysis. A.M.K., A.M., Y.M., C.Y. and L.M.-S. conducted the in vitro and in vivo live virus assessments. P.A.G. and N.B.E. acquired the clinical specimens. D.D.H., L.L., and Q.W. conducted the pseudovirus neutralization assay. J.J.K., L.M.-S., M.R.W., and D.D.H. supervised the work. M.S.P., J.J.K., L.M.-S., and M.R.W. wrote the manuscript. All authors have read and approved the manuscript.

Competing interests

M.S.P., A.M.K., A.C., M.B., S.S., S.P., N.B.E., P.A.G., M.R.W., L.M.-S., and J.J.K. are co-inventors on patent applications that include claims related to the hmAbs described in this manuscript.

Additional information

Supplementary information The online version contains supplementary material available at <https://doi.org/10.1038/s44298-024-00063-z>.

Correspondence and requests for materials should be addressed to James J. Kobie.

Reprints and permissions information is available at <http://www.nature.com/reprints>

Publisher's note Springer Nature remains neutral with regard to jurisdictional claims in published maps and institutional affiliations.

Open Access This article is licensed under a Creative Commons Attribution-NonCommercial-NoDerivatives 4.0 International License, which permits any non-commercial use, sharing, distribution and reproduction in any medium or format, as long as you give appropriate credit to the original author(s) and the source, provide a link to the Creative Commons licence, and indicate if you modified the licensed material. You do not have permission under this licence to share adapted material derived from this article or parts of it. The images or other third party material in this article are included in the article's Creative Commons licence, unless indicated otherwise in a credit line to the material. If material is not included in the article's Creative Commons licence and your intended use is not permitted by statutory regulation or exceeds the permitted use, you will need to obtain permission directly from the copyright holder. To view a copy of this licence, visit <http://creativecommons.org/licenses/by-nc-nd/4.0/>.

© The Author(s) 2024